Available online at www.sciencedirect.com
SCIENCE DIRECT
Polymer 47 (2006) 367–378
polymer
www.elsevier.com/locate/polymer

A multi-scale analysis of the microstructure and the tensile mechanical behaviour of polyamide 66 fibre

A. Marcellan [1], A.R. Bunsell, L. Laiarinandrasana *, R. Piques

Centre des Matériaux, Ecole des Mines de Paris, BP 87, 91003 Evry, Cedex, France

Received 4 February 2005; received in revised form 4 October 2005; accepted 20 October 2005
Available online 28 November 2005

Abstract

Multi-scale analyses were carried out on polyamide 66 (PA66) fibres by single fibre mechanical tests, scanning electron microscopy observations, wide-angle X-ray diffraction (WAXD) characterisation coupled with profile fitting procedure and μ-Raman extensometry. The study has attempted to reveal the microstructural parameters controlling tensile mechanical performance (i.e. stiffness and damage), to describe the micro-mechanisms of deformation involved during loading and finally to suggest a microstructural model. The main role played by isotropic amorphous regions during the first steps of deformation and the initiation of enthalpic deformation modes at higher strain levels were observed either by WAXD or μ-Raman spectroscopy. A crystallization process, induced by mechanical loading, was noted. The final deformation regime, described as viscoplastic, was seen to be activated beyond a threshold strain-value and to be due to macrofibril sliding. These coupled analyses have revealed the discontinuous character of the microfibrillar structure and have enabled a microstructural model for the fibre to be proposed.
© 2005 Elsevier Ltd. All rights reserved.

Keywords: Polyamide 66 fibres; Mechanical properties; Microstructure

1. Introduction

Polyamide 66 fibres (PA66) are complex engineering polymers used for a wide range of industrial applications. In such roles the material has to exhibit high resistance to crack initiation, which imparts high toughness to unnotched materials. Many studies have been carried out on PAs fibres in order to correlate macroscopic mechanical properties with microstructural parameters. Several microstructural models have attempted to describe the morphological architecture of semi-crystalline fibres. The microfibrillar structure of PA fibres has been largely described in the literature [1–4] and the macrofibrillar entities have been proposed by Oudet et al. [5]. The commonly used 'Swiss-Cheese' model of Prevorsek describes a parallel model in which an oriented amorphous interfibrillar phase controls stiffness and tenacity [4].

The crystalline orientation and many crystalline morphological characteristics such as index of crystallinity, degree of crystalline perfection or orientation, apparent crystallite size,… have been traditionally measured to a high accuracy and precision by wide-angle X-ray diffraction (WAXD) [6]. Thanks to the development of profile fitting procedures, amorphous domains can now be characterized in the same way as crystalline domains and permit a more accurate description of semi-crystalline structures to be made [7–15]. The significance of this procedure has been discussed in a previous paper which drew on differential scanning calorimetry and birefringence to confirm the observations [16].

Here, in a first step, the WAXD microstructural comparison by WAXD of three PA66 fibre grades has been investigated coupled with mechanical characterisation under tensile loading conditions, including strain-rates effects. Additionally, the micro-mechanisms of deformation during tensile loading have been investigated on an ultra-high performance PA66 fibre using the WAXD procedure, μ-Raman spectroscopy and scanning electron microscopy (SEM) observations.

An original micro-mechanics approach based on μ-Raman spectroscopy has been applied for the first time to a semi-crystalline system and has permitted preferentially C–C bond elongation due to the crystalline or the oriented amorphous domains to be followed.

This paper attempts to reveal the microstructural parameters, in PA66 fibres, controlling tensile mechanical performance (i.e. stiffness and damage), to describe the micro-mechanisms of deformation involved during loading and finally to suggest a microstructural model of the fibre.

* Corresponding author. Tel.: +33 1 60 76 30 64; fax: +33 1 60 76 31 50.
E-mail address: lucien.laiarinandrasana@ensmp.fr (L. Laiarinandrasana).
[1] Present address: PCSM, ESPCI, 10 rue Vauquelin, 75005 Paris, France.

0032-3861/$ - see front matter © 2005 Elsevier Ltd. All rights reserved.
doi:10.1016/j.polymer.2005.10.093

2. Materials and experimental methods

2.1. Materials

The materials of interest consisted of three grades of poly(hexamethylene adipamide) (PA66) fibres produced by Rhodia (France). Two of them were multifilaments used in tyre reinforcement, respectively called ultra-high performance fibre (UHPF) and high performance fibre (HPF), whereas the last one was a monofilament produced for textile applications (TM). TM yarns exhibit lower mechanical properties due to the fibre processing used and contain 0.4 wt%. TiO_2 fillers (particle mean size = 0.2 μm).

All type of the fibres considered had a consistent mean diameter along the fibre axis of about 30 μm.

As a first step, comparative microstructural analyses were performed on these three grades in order to better understand the effects of microstructural parameters on mechanical performance. In a second step, micro-mechanisms of deformation involved during monotonic loading were analysed on UHPF, the sample presenting the most interesting mechanical properties.

2.2. Mechanical testing and scanning electron microscopy

Single fibres were tested under controlled conditions of temperature and relative humidity (21 °C and 50% RH) with a universal testing device. The loading was monitored with an accuracy of ±0.05 g and the cross head displacement to ± 0.001 mm under tensile conditions [17]. The specimen gauge length was 50 mm. Fibre diameters were systematically measured before tests with an accuracy of 0.1 μm. Three strain rates, given in Table 1, were used in order to study viscoelastic effects during tensile loading.

Observations of the fibre surfaces after tensile or relaxation tests were made using a LEO DSM982 Gemini Field Emission Gun Scanning Electron Microscope at an acceleration voltage of 2 kV.

2.3. Wide-angle X-ray diffraction (WAXD)

Wide-angle X-ray diffraction measurements were obtained with a Siemens D500 diffractometer in the transmission mode using Co K_α radiation ($\lambda = 1.789$ Å). Detection was ensured by an Elphyse linear detector.

In order to carry out WAXD measurements under mechanical loading, a specific sample holder, maintaining individual fibres parallel to one another has been designed [18].

Table 1
Strain rates range used for mechanical characterization

Strain rates	RH	RM	RL
$d\varepsilon/dt$	400% min^{-1}	100% min^{-1}	20% min^{-1}
	6.6×10^{-2} s^{-1}	1.6×10^{-2} s^{-1}	3.3×10^{-3} s^{-1}

Yarns were first submitted to different strain levels using a tensile machine (MTS, using a force capacity of 5000 N). For each strain level of interest, the strain was maintained in the tensile machine for more than 30 min, in order to stabilize the viscoelastic component of the behaviour. After stabilisation of stress vs. time, the sample holder was then attached to the fibres at the extension level fixed by the mechanical device, removed from the tensile machine and placed directly in the X-ray goniometer. For different levels of strain, new samples were used. Only the ultra-high performance fibres, UHPF, have been analysed at different nominal strain levels: 0, 3.5 and 10%, three states of deformation noted respectively UHPF-0%, UHPF-3.5% and UHPF-10%. Beyond 10% of nominal strain, fibre failures occurred.

The scans were collected between the following diffraction angles $2\theta = 15$ and 40°. θ–2θ scans were obtained with the sample spinning in its own plane to determine orientation and evaluate the index of crystallinity. A sequence of θ–2θ scans were carried out for variants of azimuthal angle, noted φ. φ values ranged from −90 to 90°, with azimuthal increments $\Delta\varphi$ from 2.5 to 10°.

Equatorial scans, conventionally $\varphi = 0°$, were performed to determine crystalline perfection, phase proportions and apparent crystallite sizes.

2.3.1. Profile fitting procedure

The θ–2θ scans obtained at various azimuthal angles were resolved into crystalline and amorphous contribution using a profile fitting program based on the least-square procedure (Topas P, Brücker). The background was supposed linear, in order to reduce the number of parameters. Details of the detail procedure are given elsewhere [18].

After a preliminary study and inspired by recent works on PA6 fibres [7,9–12,14], the Pearson VII function was found to describe adequately and stabilise the diffracted patterns. The shape factor was fixed at 2 for all the peaks.

Near the equatorial position, two crystalline peaks, (100) and (010,110), were seen to emerge from the amorphous halo, see Fig. 1. The (100) layer and the (010,110) doublet positions were maintained fixed after an optimisation procedure of their position in an equatorial scan [18]. The parameters of the amorphous and crystalline peaks were plotted as a function of azimuthal angle ϕ, in order to determine the different microstructural characteristics.

2.4. Micro-Raman spectroscopy

Raman spectra were obtained using a Dilor 'XY' spectrometer (Lille, France) with a double holographic monochromator and X–Y micrometric plate allowing 2D displacements. The source was an Ar^+–Kr^+ ion laser (model 'Innova 70', coherent), used at a wavelength of 647.1 nm and a power of less of 15 mW (spot size ~1 μm). Aperture slits were about 60 μm. Excitation and collection were performed with an Olympus optical microscope (×1000) used under confocal conditions. Detection was ensured by a high sensitive nitrogen-cooled charge coupled (CCD) camera (2000×250 pixels with

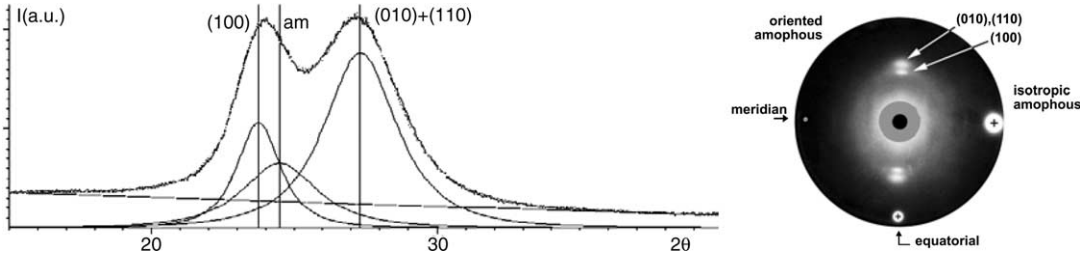

Fig. 1. WAXD equatorial ($\varphi = 0°$) θ–2θ scan resolved into amorphous (am) and crystalline ((100) and (010)+(110)) contributions. The baseline is shown as linear, (UHPF).

rear illumination), giving a resolution of 0.3 cm^{-1}. Low frequency modes have been investigated from 30 to 500 cm^{-1}. Raman scans have been treated, using mixed Lorentzian/Gaussian profile fittings in order to isolate the Rayleigh diffusion contribution on the spectra.

A single fibre was mounted in a universal fibre tester device and subjected to different strain levels. Raman spectra obtained during mechanical loading were monitored after a delay of 300 s, in order to stabilise the viscoelastic component of the behaviour. Exposure times were about 900 s. The laser was positioned in the fibre centre and focused on fibre edges in order to collect the signal from the fibre core. Scans were collected under polarisation perpendicular to the fibre axis, noted $\perp$. Details of the procedure are given elsewhere [19].

3. Results and analysis

3.1. WAXD comparative microstructural characterization of UHPF, HPF and TM

θ–2θ WAXD scans were obtained for various azimuthal angles. Fig. 1(a) and (b) shows, respectively, an example of a profile fitting of an equatorial pattern and the two dimensional X-ray diffraction image. WAXD measurements coupled with profile fitting provided information at different scales: crystalline domains and amorphous regions. The amorphous regions can more accurately be described as non-crystalline, because these domains have some degree of medium-range order, which is not expected in a truly amorphous phase. However, the term 'amorphous', distinguishing both 'isotropic' and 'oriented' amorphous domains will be used, see Fig. 1(b).

Profile results of the θ–2θ scans were plotted Fig. 2 as a function of azimuthal angle for crystalline and amorphous contributions. Results are summarised in Table 2.

3.1.1. Crystalline domains: phase identification and index of perfection

The α phase initially defined by Bunn and Garner [20] has been identified as the major phase in these fibres. Only traces of the β phase were observed at $2\theta \approx 12°$ for (002) layers reflections, and no γ phase was seen.

The description of the triclinic unitary cell α ($a = 4.9$ Å, $b = 5.4$ Å, $c = 17.2$ Å, $\alpha = 48.5°$, $\beta = 77°$, $\gamma = 63.5°$, **c** along the chain axis [20]) has been refined into α_I and α_{II} phases [21]. α_I and α_{II} phases are described as slight variations of crystallographic parameters of the α phase, the α_I phase being more highly ordered than the α_{II} phase (density of α_I and α_{II} phases are respectively, $d\alpha_I = 1.213$ g cm^{-3} and $d\alpha_{II} = 1.173$ g cm^{-3} [22]).

The index of crystalline perfection, ICP, is defined under equatorial configuration as the angular distance between the (010,110) doublet and the (100) plans:

$$\mathrm{ICP} = \theta_{(010,110)} - \theta_{(100)} \tag{1}$$

The ICP was estimated for all grades and interpreted in terms of the ratio of α_I and α_{II} phases. Therefore, it is assumed that crystalline perfection was directly proportional to the theoretical crystalline perfection of α_I and α_{II} crystals ($\Delta\theta_{\alpha I} = 1.75°$, $\Delta\theta_{\alpha II} = 0.42°$, with Cu K_α radiation [21]). The α_I phase was largely predominant in all samples, with TM yarns showing slightly less α_I phase.

3.1.2. Crystalline domains: apparent crystallite size (ACS)

Profile analysis of equatorial scans was used to obtain an apparent crystallite size, ACS_{hkl} in the normal direction of (hkl) layers using the Scherrer's formula [23]:

$$\mathrm{ACS}_{hkl} = \frac{0.9\lambda}{\Delta\theta_{hkl} \cdot \cos\theta_{hkl}} \tag{2}$$

In which λ is the wavelength, θ the peak position and $\Delta\theta_{hkl}$ the full-width at half-maximum of crystalline peak.

WAXD measurements only gave an average value for ACS, see Table 2. However, WAXD results for equatorial scans show slightly smaller ACS_{100} in the TM sample than in the UHPF and HPF samples. Moreover, according to Fig. 2(b), the apparent crystallite size, ACS_{100} is a maximum at the equator and the larger crystallites seem to be oriented along the fibre axis during processing. The same trend is observed for all samples. Nevertheless, the UHPF seems to present the narrowest distribution of ACS_{100}.

DSC thermograms have also been published elsewhere [16] and give an indication of crystallite size or crystallite distortions based on the melting temperature. DSC measurements clearly confirmed ACS interpretations: two melting behaviours have been revealed and interpreted in terms of crystallite size distribution. UHPF and HPF samples contained similar crystallite morphologies (with respect to a broad endothermic peak at $\cong 257.5$ °C), whereas, TM presented an additional majority peak at the lower melting temperature ($Tf \cong 250.2$ °C).

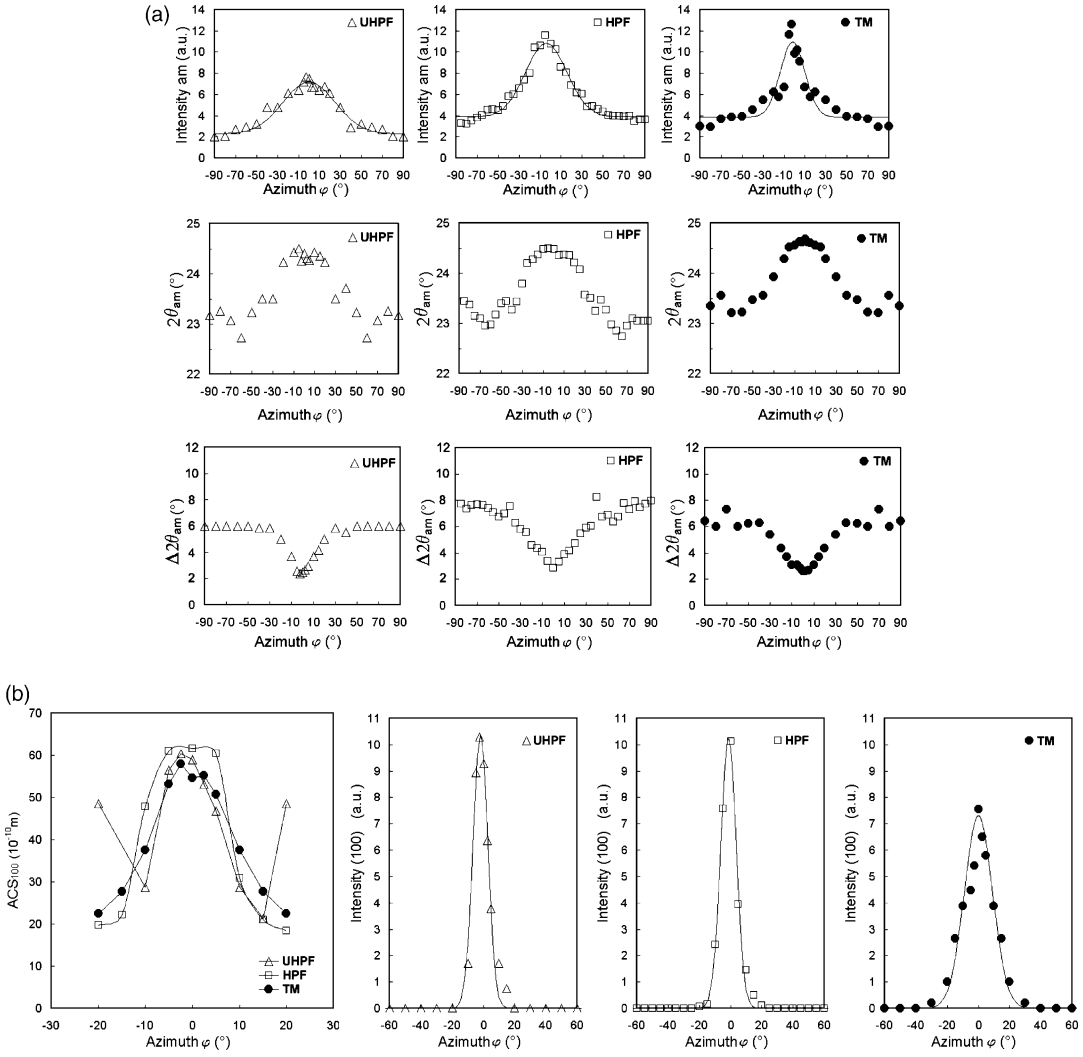

Fig. 2. Comparison of UHPF, HPF and TM grades: WAXD peak parameter evolutions. (a) Variations in the amorphous domain: intensity, amorphous position ($2\theta_{am}$) and full-width at half maximum ($\Delta 2\theta_{am}$) with the azimuthal angle. (b) Variations in the crystalline domain: apparent crystallite size (ACS_{100}), intensity (100) with the azimuthal angle.

Table 2
Comparative microstructural results: UHPF, HPF and TM (see text for symbol explanation)

Mechanical performance microstructural analysis		UHPF ultra-high performance	HPF high performance	TM textile monofilament
WAXD	α_l%	83(±1.5)	83(±1.5)	76(±1.5)
	X_c%	46(±2)	39(±2)	44(±2)
	X_{oa}%	23(±1)	20(±1)	13(±1)
	X_{ia}%	31(±1)	41(±1)	43(±1)
	F_{oa}	0.42	0.33	0.23
	$f_{c,z}$	0.980(±0.005)	0.978(±0.005)	0.929(±0.005)
	$f_{am,z}$	0.655(±0.01)	0.651(±0.01)	0.639(±0.02)
	$f_{oa,z}$	0.783(±0.01)	0.857(±0.01)	0.942(±0.02)
	ACS_{100} (Å)	55(±1)	58(±1)	51(±1)
	$2\theta_{am,\phi=0°}$	24.41°(±0.1)	24.48°(±0.1)	24.68°(±0.1)
DSC	$X_{c\ DSC}$%	45(±0.3)	41(±2.8)	44(±0.6)
	Tf (°C)	257.6(±0.0)	257.3(±1.1)	250.6(±0.6)/257.6(±0.8)
Birefringence	Δ (10^{-3})	61.6(±0.7)	60.0(±1.2)	55.3(±1.1)
	$f_{am,z}$*–**	0.505–0.749	0.511–0.727	0.407–0.636

*–** The value of $f_{am,z}$ was determined using the intrinsic optical birefringence of amorphous and crystalline domains: $^{*}\Delta^{\circ}_{c}=0.096$ et $^{*}\Delta^{\circ}_{a}=0.077$ [25] et pour $\Delta^{\circ}_{c}=\Delta^{\circ}_{a}=0.073$ [26].

Table 3
Evolution of microstructural parameters during tensile loading: UHPF-0%, UHPF-3.5% and UHPF-10%.

Strain level microstructural domains		UHPF-00%	UHPF-3.5%	UHPF-10%
Crystallites	ICP (min)	91.6(±1.2)	90.1(±1.2)	84.2(±1.2)
	ACS_{100} (Å)	55(±1)	56(±1)	48(±1)
	$f_{c,z}$	0.980 (±0.005)	0.975 (±0.005)	0.983 (±0.005)
	X_c%	46(±2)	51(±2)	54(±2)
Amorphous	$2\theta_{am,\phi=0°}$	24.41°	24.66°	24.56°
	$2\theta_{am,\phi=90°}$	23.17°	22.70°	22.60°
	F_{oa}	0.42	0.47	0.49
	X_{ia}%	31(±1)	26(±1)	23(±1)
	X_{oa}%	23(±1)	23(±1)	23(±1)
	$f_{oa,z}$	0.783 (±0.01)	0.865 (±0.01)	0.869 (±0.01)
	$f_{am,z}$	0.655 (±0.01)	0.691 (±0.01)	0.718 (±0.01)

3.1.3. Crystalline domains: orientation

The degree of orientation was calculated as the Hermans orientation factor [24]:

$$f_\phi = \frac{1}{2}(3\langle\cos^2\phi\rangle - 1) \quad (3)$$

with ϕ, the angle between normal of crystal planes diffracting and the reference fibre axis, z ($\phi = \pi/2 - \varphi$). The mean $\cos^2\phi$ was determined from the following expression, assuming rotational symmetry about the fibre axis:

$$\langle\cos^2\phi\rangle = \frac{\int_0^{II/2} I(\phi)\sin\phi\cos^2\phi \mathrm{d}\phi}{\int_0^{II/2} I(\phi)\sin\phi \mathrm{d}\phi} \quad (4)$$

with $I(\varphi)$, diffracted intensity at φ.

Intensity variations were fitted with a gaussian peak shape, see Fig. 2(a) and (b). Hermans orientation factor being equal to 0 for a random distribution, 1 for a total alignment of the identities and −1/2 if all were perpendicular to the fibre axis.

This function was also applied to calculate the orientation of amorphous domains $f_{am,z}$ (including the baseline) and $f_{oa,z}$ (subtracting the isotropic component), see Table 2.

Crystalline domains of the three samples were seen to be parallel to the fibre axis and reached very high values of ordering (more than 0.9, cf. Table 2).

The ultra-high and high performance fibres, UHPF and HPF, have revealed higher values of crystalline orientation (respectively, 0.980 and 0.978), compared to the textile monofilament TM (0.929).

3.1.4. Crystalline domains: index of crystallinity

The crystallinity index, X_c, was defined as the ratio between the intensity diffracted by crystalline regions and the total intensity diffracted integrated over the φ directions, following previous works of Murthy et al. [9–12].

Crystalline indices showed a high degree of crystallisation for our samples, with fibres UHPF and TM near to the maximum of crystallinity.

As it is shown in Table 2, the X_c values obtained by WAXD are in good accordance with the melting enthalpy measurements carried out elsewhere by DSC [16], and validate our profile fitting method.

3.1.5. Amorphous regions: indices and orientation

The evolution of amorphous peak parameters shown in Fig. 2(a) such as intensity (I_{am}), full-width at half-maximum ($\Delta\theta_{am}$) and position ($2\theta_{am}$) reveal that part of the amorphous domain depends on orientation.

Changes in the position of the amorphous halo, with a maximum value for equatorial scans show that this amorphous phase consists of denser oriented and less dense isotropic regions.

X_{oa}, index of oriented amorphous domain and X_{ia}, index of isotropic amorphous domain were defined from peak intensity variations $I(\varphi)$ assuming that the isotropic amorphous component remained independent of the φ angle (under the baseline, see Fig. 2(a)). Quantification of the isotropic amorphous and oriented amorphous regions remained the prime interest of the WAXD measurements coupled with profile fitting. The fraction of amorphous phase which was oriented, F_{oa}, was also defined as the ratio between X_{oa} and X_{ia}.

The ultra-high performance fibre, UHPF, presented the maximum value of F_{oa}, followed by HPF and TM. The X_{oa} index seems to be quite similar for both UHPF and HPF fibres.

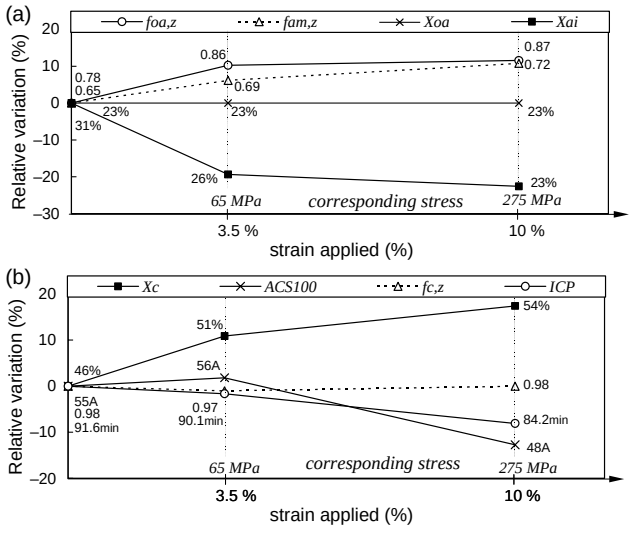

Fig. 3. Relative variations during loading for (a) amorphous parameters and (b) crystalline parameters.

The amorphous orientation function, $f_{am,z}$, and the oriented amorphous function, $f_{oa,z}$ were calculated using the Hermans orientation factor. The $f_{oa,z}$ function was calculated considering the diffracted amorphous intensity, subtracting the baseline.

It should be noted that the UHPF fibres show the highest global amorphous orientation (0.655) despite the lowest orientation degree of oriented amorphous domains (0.783).

The amorphous orientation function has also been evaluated elsewhere [16] using birefringence measurements in order to confirm the WAXD method of calculating $f_{am,z}$, see in Table 2.

3.2. WAXD analysis of microstructural parameters evolution during tensile loading (UHPF)

Microstructural evolution during loading was studied by WAXD. UHPF have been analysed at different nominal strain levels: 0, 3.5 and 10%, three states of deformation noted respectively UHPF-0%, UHPF-3.5% and UHPF-10%. Results are summarized in Table 3 and in Fig. 3.

3.2.1. Amorphous regions: density, indices and orientation

The evolution of amorphous peak parameters such as the intensity (I_{am}), the full-width at half-maximum ($\Delta\theta_{am}$) and the halo position ($2\theta_{am}$) are shown in Fig. 4(a).

In the equatorial position, the amorphous halo position revealed a weak sensitivity with respect to mechanical strain. No compaction effect of the oriented amorphous regions was seen. Whereas, in the meridian position, the peak position was shifted significantly in the small angle direction between UHPF-0% and UHPF-3.5%, and then is stabilized between UHPF-3.5% and UHPF-10%.

As shown in Fig. 3(a), the evolution of the isotropic amorphous index, X_{ia}, was seen to be very clear: a large decrease is observed between UHPF-0% and UHPF-3.5%

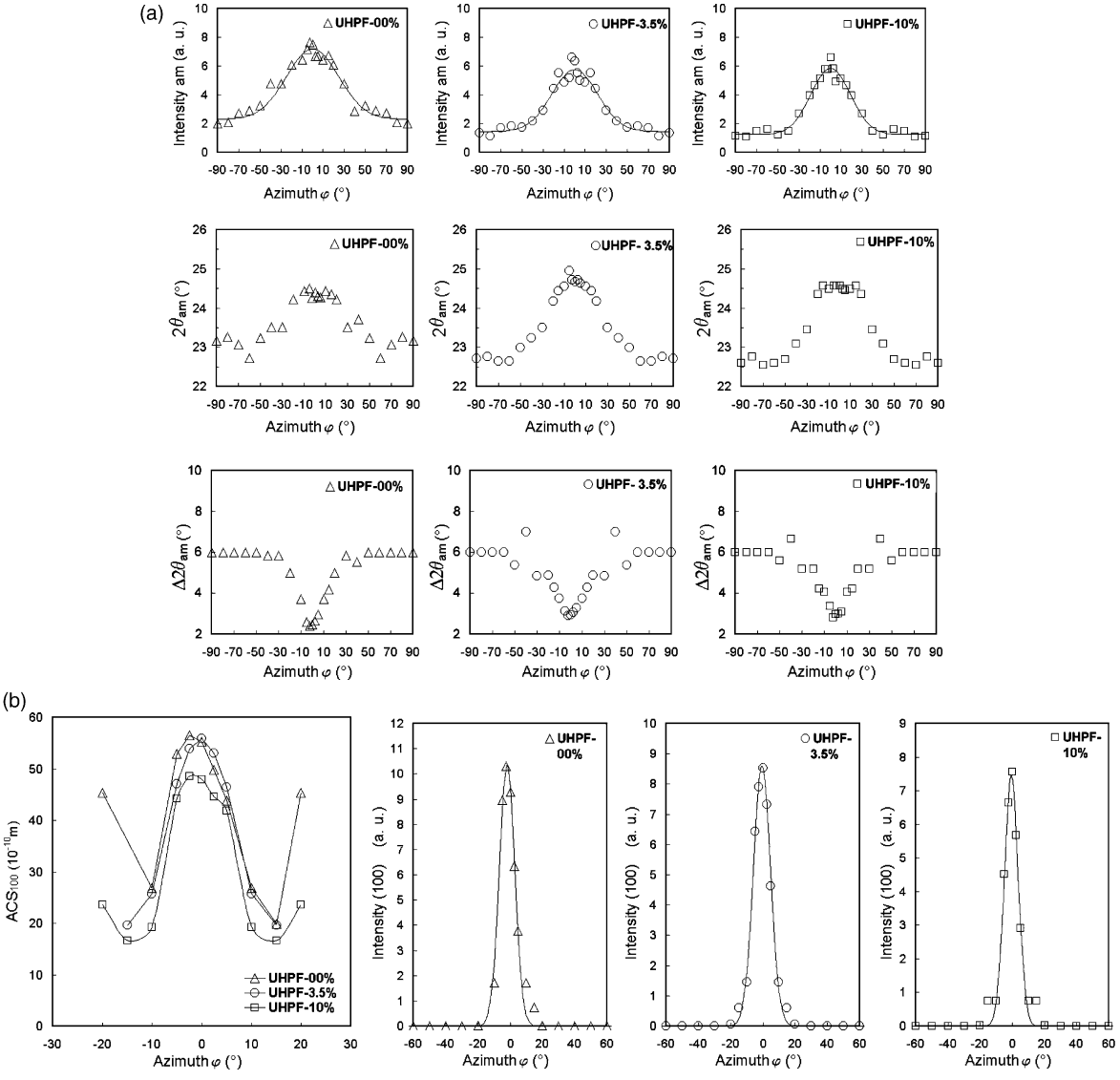

Fig. 4. Micro-mechanisms of deformation: WAXD peak parameter evolutions for UHPF-00%, UHPF-3.5% and UHPF-10%. (a) Variations in the amorphous domain: intensity, amorphous position ($2\theta_{am}$) and full-width at half maximum ($\Delta 2\theta_{am}$) with the azimuthal angle. (b) Variations in the crystalline domain: apparent crystallite size (ACS_{100}), intensity (100) with the azimuthal angle.

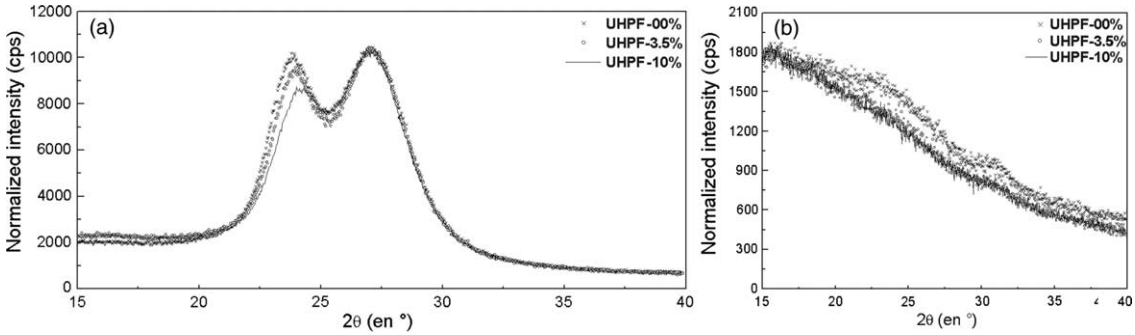

Fig. 5. Comparison of WAXD scans at different strain levels for (a) the equatorial position, $\varphi = 0°$ or (b) the meridian position, $\varphi = 90°$. Scans have been normalized with respect to the background.

(from 31 to 26%) and then a slight decrease between UHPF-3.5% and UHPF-10% (from 26 to 23%). Non-deconvoluted diffractogramms under meridian configuration are shown in Fig. 5 for UHPF-0%, UHPF-3.5% and UHPF-10%. Moreover, the independence of the X_{oa} according to the applied strain level should be noted (Fig. 3(a)).

Concerning amorphous orientation, the relevant parameter concerning the amorphous orientation was $f_{oa,z}$ because of its independence versus the index of isotropic amorphous domains. Large reorientation steps in the orientated amorphous regions were noted during loading, see in Fig. 3(a).

3.2.2. Crystalline domains: crystalline perfection, ACS, orientation and index

The index of crystalline perfection, ICP, defined under equatorial configuration as the angular distance between the (010,110) doublet and the (100) plans, has been seen not to significantly change when comparing UHPF-0% and UHPF-3.5%, from 91 to 90 min, whereas, the parameter clearly decreased between UHPF-3.5% and UHPF-10%, from 90 to 84 min (Fig. 3(b)). The higher the applied strain, the more disturbed the crystalline domains oriented along the fibre axis. An overlay of non-deconvoluted equatorial diffractograms is shown in Fig. 5. An apparent shift of (100) peak is shown with respect to the relative stability of the (010,110) doublet. This displacement seems to correspond to a lateral compaction along the **a**-axis (hydrogen bond direction) induced by the loading of the macromolecular chains oriented along the fibre axis. On the other hand, the interlayer distance $d_{010,110}$ remains constant, caused by the low energy bonding of the Van der Waals interactions (**b**-direction).

As for the apparent crystallite size, ACS_{100}, it can be seen from Fig. 3(b), that the ACS_{100} was quite similar between UHPF-0% and UHPF-3.5%. At UHPF-10%, the ACS_{100} decreased greatly, involving lamella damage in the hydrogen bonding direction (disruption or distortions of the unit cells along the crystallographic **a**-axis).

Moreover, the ACS_{100} distribution was seen to be narrower at UHPF-10% than at UHPF-3.5% and at UHPF-0% (Fig. 4(b)).

The index of crystallinity, X_c, revealed a sensitive increase during mechanical loading (Fig. 3(b)). A large increase between UHPF-0% and UHPF-3.5% (from 46 to 51%) and an incremental increase for UHPF-10% (54%) was noted. Using profile-fitting methods, this trend has been already reported by authors on PA6 fibres submitted to different draw ratios [11,14]. Moreover, the crystalline orientation was seen to remain constant at the applied strain levels.

3.3. Micro-Raman extensometry of crystalline and oriented amorphous C–C chains (UHPF)

Information at the scale of chemical bonds (0.1–1 nm) was provided by μ-Raman spectroscopy. Several micro-mechanical studies have already been carried out but only dealing on highly oriented systems [27–29] such as PBO fibres, aramid fibres, high modulus PE, etc. For the first time, the μ-Raman spectroscopy is here dedicated to the micro-mechanical study of a semi-crystalline system.

The prime interest of the Raman spectrometry investigation was to follow crystalline and oriented amorphous C–C chain elongation during tensile loading through the collective skeletal motions at $\sim 100\,cm^{-1}$. In this way, μ-Raman spectroscopy has been used as a μ-Raman extensometer of the crystalline and the oriented amorphous domains. Details of the determination of the vibrational mode and the suitability

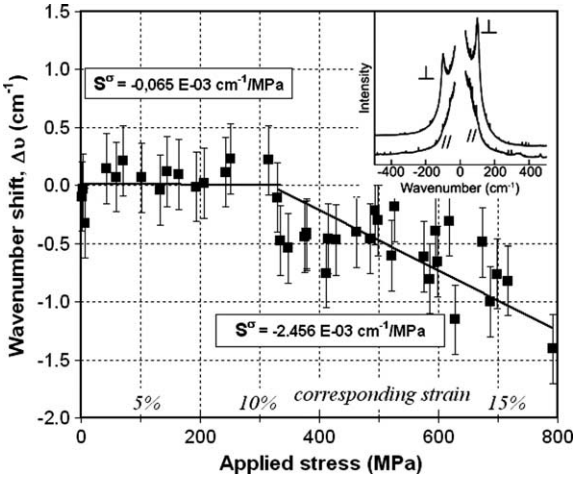

Fig. 6. Micro-Raman extensometry: wavenumber shift plotted as a function of increasing applied stress, showing onset of main crystalline and oriented amorphous chain deformation at an applied stress of around 350 MPa, (UHPF).

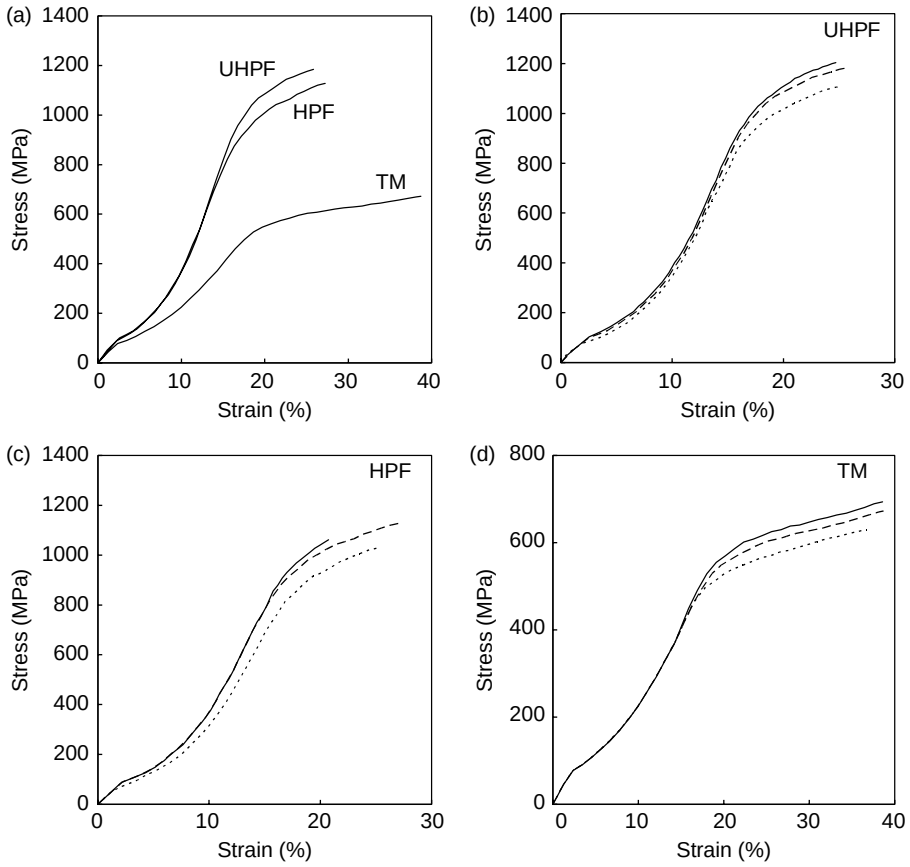

Fig. 7. Typical tensile stress–strain curves: (a) mechanical behaviour of UHPF, HPF and TM at a strain rate of RM: $1.6\times10^{-2}\,s^{-1}$; (b)–(d) strain-rate effect at RH: $6.6\times10^{-2}\,s^{-1}$, RM: $1.6\times10^{-2}\,s^{-1}$ and RL: $3.3\times10^{-3}\,s^{-1}$, respectively, for UHPF, HPF and TM.

of the $100\,cm^{-1}$ band for μ-Raman extensometry are given elsewhere [19].

The vibrational response as shown in Fig. 6 was highly polarized and confirmed the high degree of orientation of the system (for parallel polarisation to the fibre axis, noted ∥, or perpendicular, ⊥).

The UHPF fibre was held in the mechanical device. Spectra were systematically recorded at the UHPF fibre centre after stress stabilisation versus time, according the procedure described above. Two important stages of mechanisms of deformation can be seen in Fig. 6: first a plateau is observed up to a threshold of about 350 MPa and then a shift downwards is obvious. For simplicity the relationship is represented as a straight line:

$$\Delta\nu = \nu_0 + S^{\sigma}\times\sigma \tag{5}$$

with $S^{\sigma} = -2.46\times10^{-3}\,cm^{-1}\,MPa^{-1}$.

The initial plateau behaviour is consistent with the alignment of the macromolecules of amorphous regions: amorphous regions accommodate strain up to 350 MPa with no influence on the wavenumber, which implies few entanglements of the amorphous domains. Above 350 MPa, the load is then also supported by the crystalline phase and oriented amorphous regions, from which an influence on the spectra can be observed, indicating that crystalline and oriented amorphous C–C bonds are loaded.

3.4. Mechanical properties and scanning electron microscopy examinations

3.4.1. General mechanical behaviour and UHPF, HPF, TM comparison

Typical strain stress curves of UHPF, HPF and TM fibres are shown Fig. 7(a) for the medium strain rate RM ($1.6\times10^{-2}\,s^{-1}$).

The general tensile behaviour is similar for all samples. The mechanical behaviour is highly non-linear and presents three main domains defined by a changing concavity. The first part of the curves, near the origin, is quite linear and the initial modulus E_i is defined. The E_i values are quite similar for all samples and vary from 4.0 GPa for TM to 4.8 GPa for HPF and 5.3 GPa for UHPF. Beyond 2% strain, the curves present a rubber-like 'S' shape. The progressive stiffening of the fibre during loading is interpreted as being entropic or rubber-like behaviour, reflecting the progressive alignment of molecules. The last deformation regime presents a curve with a 'plateau' shape and leads to the final failure of the fibre.

Tensile tests were conducted at three strain rates: RH ($6.6\times10^{-2}\,s^{-1}$), RM ($1.6\times10^{-2}\,s^{-1}$) and RL ($3.3\times10^{-3}\,s^{-1}$), see Fig. 7(b)–(d). For all samples a significant strain rate dependence revealed the viscoelastic component of the mechanical behaviour under the room temperature ($T-T_g = -20\,°C$). The strain-rate effect is noted to be present from the

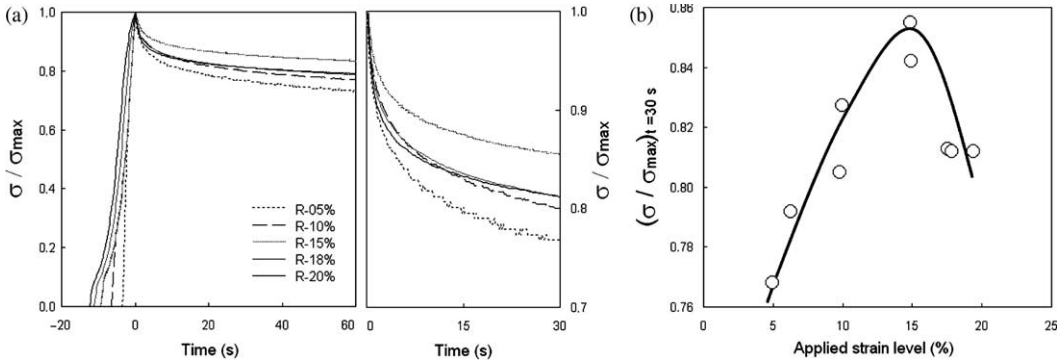

Fig. 8. (a) Typical relaxation curves for different applied strain levels: R-05%, R-10%, R-15%, R-18% and R-20%. The strain rate used to attain the strain set point is RM: $1.6\times10^{-2}\,s^{-1}$. The time reference, $t=0$ s, is taken to be equal to zero when the required applied strain level is attained. Curves are normalized using the parameter σ/σ_{max}, with σ_{max} equal to the maximum stress value (i.e. for $t=0$ s). (b) Stress relaxation ratio σ/σ_{max} versus applied strain level indicating two different viscous mechanisms.

beginning of the UHPF, HPF curves (Fig. 7(b) and (c)). The viscoelastic behaviour of TM is seen Fig. 7(d) to be quite different and seems to be induced after 15% strain.

3.4.2. Stress relaxation: definition of a viscoplastic threshold

Stress relaxation tests consist in maintaining a fixed strain level and in recording the mechanical response of the material history. Tests are carried out for various strain levels from R-05% to R-20%, as shown Fig. 8.

A fixed strain rate is used to attain the applied strain for all samples (RM: $1.6\times10^{-2}\,s^{-1}$). Therefore, the time needed to reach the imposed strain level is different for each strain level. The time reference is taken to be equal to 0 when for the first time the imposed strain is attained. Curves are also normalized using the parameter σ/σ_{max}, with σ_{max} equal to the maximum stress value (i.e. for $t=0$ s).

Fig. 8(a) shows the stress relaxation evolution, in terms of both instantaneous stress (σ) and stress relaxation ratio (σ/σ_{max}). Fig. 8(b) plots the trends of (σ/σ_{max}) at $t=30$ s with respect to the applied strain. Two different mechanisms of viscosity are observed in Fig. 8(b). Tests conduced between R-05% and R-15% show that the stress relaxation ratio (σ/σ_{max}) increases with the applied strain level. This viscoelastic mechanism can be attributed to the stress relaxation involved during the delay needed to attain the strain level: the longer the delay, the more important the cumulated viscous strain at $t=0$ s. A second mechanism was noted beyond R-15%, since the R-18% and R-20% curves revealed relaxation ratio (σ/σ_{max}) clearly lower than for R-15%. The activation of a second viscous mechanism is therefore, deduced and can be assumed to be viscoplasticity.

Two viscous mechanisms have been revealed: the first, assumed to be linear viscoelasticity, and the second, assumed to be viscoplastic activated beyond a threshold (about 15% strain).

This second viscous mechanism can be related, at the fibre scale, to macrofibril sliding, failure or disentanglements, as shown in the micrograph Fig. 9. Macrofibrillar disruptions can be seen to appear along the fibre at the fibre surface beyond 15% of strain suggesting large movements in the fibre structure at the molecular level.

Relaxation tests carried out for levels superior to 15% strain rapidly led to fibre failure.

4. Discussion

4.1. Microstructural parameters controlling mechanical performance

Comparison of the UHPF, HPF and TM fibres at the microstructural scale or at the mechanical scale has revealed two types of behaviour. Two groups have been distinguished:

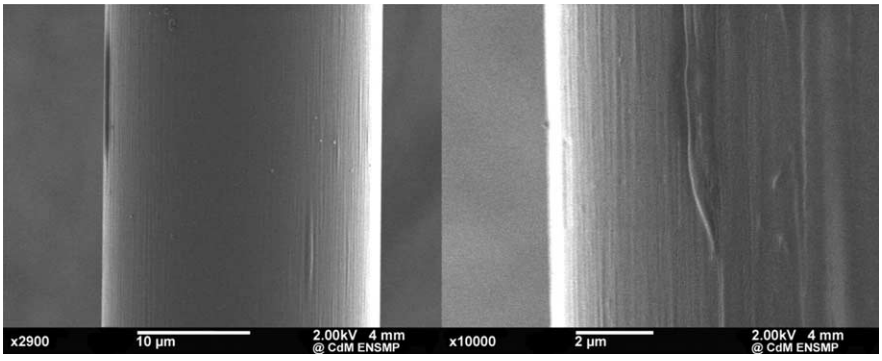

Fig. 9. Damage inducing the uplifting of the macrofibrillar structure of the fibre. SEM micrographs.

the first corresponding to the technical fibres (UHPF and HPF), the second, corresponding to the textile monofilament (TM), see typical tensile stress–strain curves in Fig. 7.

The TM fibre presents the particularity of possessing a population of crystalline lamella with an averaged size smaller than in the technical samples. Despite a very high crystallinity index, the degree of order of these crystalline regions is poor compared to the technical fibres. These features are explained by the additional TiO_2 particles introduced in the TM fibre, inducing a heterogeneous crystalline growth (i.e. high crystallinity, low ordering with distortions or smaller crystalline areas). Moreover, the X_{ia} index is the highest and the F_{oa}, fraction of oriented amorphous phase, the lowest. The oriented amorphous domains identified are at the same time the densest ($2\theta_{am,\phi=0°}=24.68°$) and the most oriented ($f_{oa,z}\sim0.94$), see Table 2.

As for the technical fibres, UHPF and HPF, their mechanical and their microstructures are very similar. The indices of crystallinity are high, with a value slightly inferior for the HPF. The X_{oa} is the same in both cases, nevertheless with F_{oa} clearly higher for the UHPF fibre (UHPF $\sim$0.42 and HPF $\sim$0.33). Finally, the values of $f_{oa,z}$ and the densities for the oriented amorphous domains are a minimum for the ultra-high performance fibre, UHPF.

In addition to the consequence of the crystalline phase (index and orientation) on the mechanical behaviour, the X_{oa} and F_{oa} parameters, respectively the index and the fraction of oriented amorphous phase, appeared to be good criteria for describing the mechanical properties of fibres (i.e. mechanical stiffness).

Moreover, the comparison of the three microstructures has revealed an unexpected feature concerning the oriented amorphous domains. It should be noted that the most oriented ($f_{oa,z}\sim0.94$) and the densest ($2\theta_{am,\phi=0°}=24.68°$) oriented amorphous domains were found for TM, see Table 2. In contrast, the UHPF fibre possessed the least oriented ($f_{oa,z}\sim0.78$) and the least dense ($2\theta_{am,\phi=0°}=24.41°$) amorphous domains. In this way the fibre is able to absorb the effects of excess straining and reduces the damage mechanisms at the molecular level. Oriented amorphous regions seem to be identified as the weakest microstructural link of the fibre responsible for fracture initiation.

4.2. Micro-mechanisms of deformation and microstructural model

From macro- to nano-mechanisms of deformation, the mechanical analysis, WAXD and micro-Raman spectroscopy measurements indicate the same micro-mechanisms induced under mechanical loading. This is illustrated in Fig. 10 which shows, schematically, the micro-mechanisms of deformation.

For small strain levels (from 0 to 3.5%), strain accommodation is ensured by the progressive alignment of the amorphous regions, whereas crystalline regions seem to remain unloaded. Isotropic amorphous domains have revealed the highest sensitivity to initial loading: the index of isotropic amorphous domains, X_{ia}, greatly decreases (from 31 to 26%) in order to add to the amount of oriented amorphous regions, X_{oa}, see summarized results in Table 3 and Fig. 3. Oriented amorphous domains are subjected to reorientation ($f_{oa,z}$ increases from 0.78 to 0.86), but their density remain unchanged. The index of crystallinity, X_c, shows a significant increase (from 46 to 51%) thanks to the 'crystallisation' of oriented amorphous domains. Macromolecular chains seem to contribute to crystalline growth along the crystallographic **c**-axis, which is the direction of crystallisation induced during the spinning process [30]. It is interesting to note that the

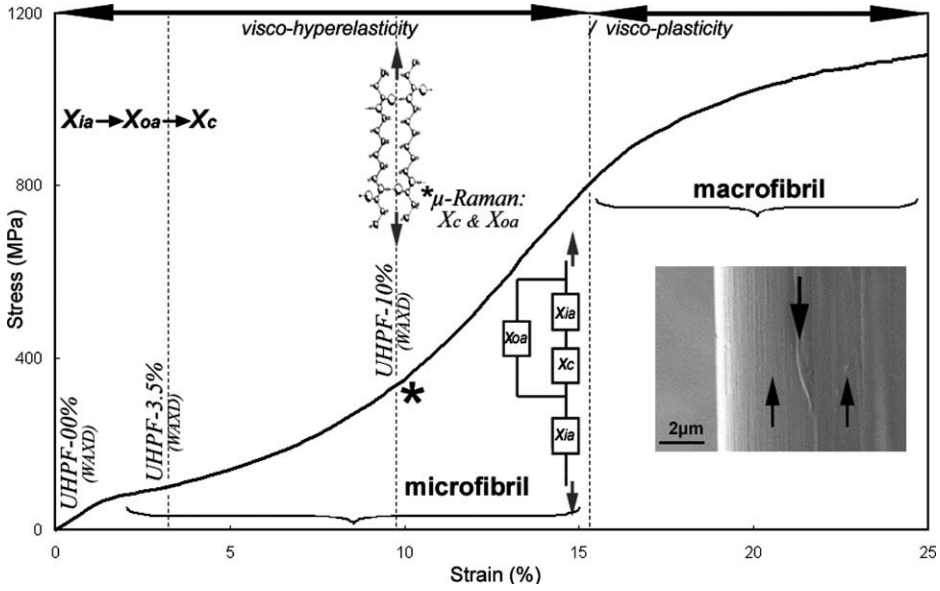

Fig. 10. Schematic representation of the micro-mechanisms involved in fibre deformation. For strain range from 0 to 3.5%, the strain accommodation is mainly ensured by the alignment of isotropic amorphous domains: isotropic amorphous phase is transformed into oriented amorphous phase which can itself change into crystalline phase. From 3.5 to 10%, the end of alignment of amorphous domains is observed. Above 330 MPa, enthalpic mechanisms are activated: C–C bonds belonging to crystalline or oriented amorphous regions are elongated. Crystalline domains are affected by the loading: ACS and ICP decrease. Above 15% strain, viscoplastic mechanism seems to be connected to macrofibril sliding. Damage at the macrofibril scale is noted at the fibre surface.

fraction of oriented amorphous phase, F_{oa}, remains insensitive to strain.

For higher stress–strain levels, above 330 MPa, enthalpic mechanisms are activated: macromolecular chains belonging to crystalline or oriented amorphous regions initiate their extension and C–C bonds are loaded (Fig. 6). Although the crystalline orientation remains stable, crystalline domains reveal modifications: ACS_{100} and crystalline perfection, ICP, are seen to decrease (from 90.1 to 84.2 min), Table 3 and Fig. 3. Under C–C chain extension, a lateral compaction along the H bond direction (**a**-axis) is induced and (100) layers are brought closer. The crystallinity index, X_c, undergoes an additional increase. At the same moment, amorphous domains finish their extension, becoming more aligned: the X_{ia} decreases from 26 to 23%. The F_{oa} remains constant and the orientation of oriented amorphous domains is not seen: $f_{oa,z}$ is stabilized at a value of 0.86/0.87.

At a mechanical scale, the behaviour is assumed to be 'rubber-like' coupled with viscoelastic behaviour which seems to be controlled by the microfibrils.

Finally, above 15% strain, viscoplasticity mechanisms are activated. At the fibre scale, on the fibre surface many ruptures of macrofibril are seen. This viscoplastic mechanism seems to be connected to the sliding of macrofibrils with respect to one another.

In the analysis carried out in this paper, information concerning the long distance arrangement of the microstructural parameters (crystalline regions, isotropic and oriented amorphous domains) has not been investigated. Nevertheless, it is interesting to discuss and compare the existing microstructural models which can be found in the literature and to analyse their implications with our results. In a recent paper Prevorsek and et al. [4] have compared the main microstructural models of nylon fibres. According to the authors Prevorsek's model seems to be the most suitable for high performance PA66 fibres: the oriented amorphous domains are supposed to control mechanical performance (i.e. stiffness and toughness). As shown in Fig. 11, Prevorsek modelled the microstructural arrangement as a parallel model interconnected with crystalline and isotropic amorphous regions. The results presented in this paper reveal an important accommodation of deformation ensured by the isotropic amorphous domains. These conclusions suggest another microstructural arrangement, Fig. 11. In this model the microfibril is considered to be discontinuous and embedded in an isotropic amorphous matrix.

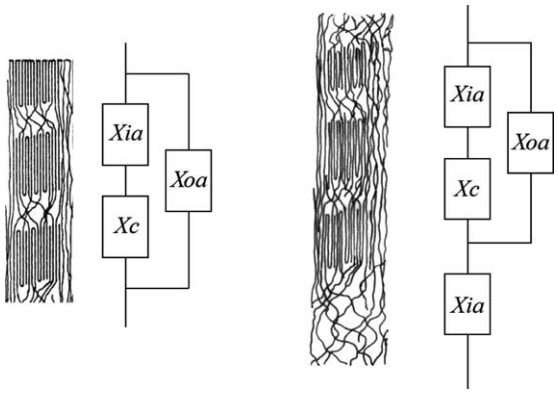

Fig. 11. Comparison of the Prevorsek parallel model and the proposed microstructure.

5. Conclusions

The multi-scale analysis carried out in this study through single fibre mechanical tests, scanning electron microscopy observations of the fibre surface, WAXD characterisation coupled with profile fitting procedure and μ-Raman extensometry sheds new light on the relationships between the microstructure and tensile mechanical behaviour of PA66 fibres.

At the fibre scale to the C–C skeletal movements, several points are significant:

- During initial deformation, strain accommodation is mainly ensured by the isotropic amorphous domains. Partial further crystallisation under load is induced by the alignment of oriented amorphous regions. At a mechanical scale the behaviour is assumed to be viscohyperelastic.
- As loading continues, C – C bonds belonging to the oriented amorphous domains and crystalline regions are elongated and control the progressive stiffening of the mechanical behaviour. Enthalpic mechanisms of deformation are activated.
- The last deformation regime, described as viscoplastic, is finally activated beyond a threshold (last inflexion in the loading curve) and seems to be linked to macrofibril sliding. Damage and reinforcement induced by alignment (analogous to stress hardening) are competing mechanisms.
- Besides the effect of crystalline domains (index and orientation) on the mechanical stiffness, the index of oriented amorphous phase, X_{oa} and the fraction of oriented amorphous phase, F_{oa} in the fibre appears also to be good criteria for predicting mechanical stiffness.
- The oriented amorphous domains seem to be identified as the microstructural weakest-link parameter in the fibre. In this way, an ideal fibre would contain large amounts of well-ordered crystallites and a high value of F_{oa}, but would also possess relative low orientation and low dense oriented amorphous domains in order to mitigate damage processes.
- The analysis carried out in this study based on a number of techniques allows to propose a new microstructural model, slightly modifying the well-known Prevorsek's model. In the proposed model the microfibril is considered to be discontinuous and connected by isotropic amorphous domains.

Acknowledgements

Dr Colomban is acknowledged for many useful discussion and his scientifical support on Raman spectroscopy. The authors wish to thank Rhodia for the supply of fibres, for their

financial support and Dr L. Nasri (Rhodia-Industrial Yarns, Swiss) and Dr G. Robert (Rhodia-CRL, France) for their close collaboration in this study. Mr Y.Favry, Mr D. Pachoutinski and Mr JC. Teissedre for their technical assistance and discussion.

References

[1] Statton WO. J Polym Sci 1959;41:143–55.
[2] Peterlin A. J Polym Sci (C) 1967;18:123–32.
[3] Prevorsek DC. Polym Sci Symp 1971;32:343–75.
[4] Bukosek V, Prevorsek DC. Int J Polym Mater 2000;47:569–92.
[5] Oudet C, Bunsell AR. J Mater Sci 1987;22:4292–8.
[6] Alexander LE. X-ray diffraction methods in polymer science. New York: Wiley; 1969.
[7] Heuvel HM, Huisman R, Lind KCJB. J Polym Sci, Polym Phys Ed 1976; 14:921–40.
[8] Heuvel HM, Huisman R. J Appl Polym Sci 1981;26:713–32.
[9] Murthy NS, Minor H. Polymer 1990;31:996–1002.
[10] Murthy NS, Minor H, Bednarczyk C, Krimm S. Macromolecules 1993; 26:1712–21.
[11] Murthy NS, Bray RG, Correale ST, et al. Polymer 1995;36:3863–73.
[12] Murphy NS, Zero K. Polymer 1997;38:2277–80.
[13] Galeski A, Argon AS, Cohen RE. Macromolecules 1991;24:3945–52.
[14] Ponnouradjou A, Piques R, Bunsell AR, Renard J, Durand M. J Phys IV 1998;8:P5.
[15] Jolly L, Tidu A, Heizmann JJ, Bolle B. Polymer 2002;43:6839–51.
[16] Marcellan A, Bunsell AR, Piques R, Colomban Ph. J Mater Sci 2003;38: 2117–23.
[17] Bunsell AR, Hearle JWS. J Appl Polym Sci 1971;18:267–91.
[18] Marcellan A. PhD Thesis. Ecole des Mines de Paris, France; 2003.
[19] Marcellan A, Colomban Ph, Bunsell AR. J Raman Spectrosc 2004;35: 308–15.
[20] Bunn CW, Garner EV. Proc R Soc, London A 1947;189:39–70.
[21] Haberkorn H, Illers KH, Simak P. Polym Bull 1979;1:485–90.
[22] Starkweather HW, Zoller P, Glover A. J Polym Sci, Polym Phys Ed 1984; 22:1615–21.
[23] Wilchinsky Z. J Appl Phys 1959;30:792.
[24] Hermans JJ, Hermans PH, Vermaas D, Weidinger A. J Polym Sci 1948;3: 1–9.
[25] Davis GT, Taylor HS. Textile Res J 1965;35:405–11.
[26] Culpin MF, Kemp KW. Proc Phys Soc 1957;69:1301–8.
[27] Young RJ, Lu D, Day RJ, Knoff WF, Davis HA. J Mater Sci 1992;27: 5431–40.
[28] Andrews MC, Lu D, Young RJ. Polymer 1997;38:2379–88.
[29] Berger L, Kausch HH, Plummer CJG. Polymer 2003;44:5877–84.
[30] Magnet C. PhD Thesis. Ecole des Mines de Paris, France; 1993.